Sustainable Energy & Fuels

ROYAL SOCIETY OF CHEMISTRY

PAPER

View Article Online
View Journal | View Issue

Cite this: *Sustainable Energy Fuels*, 2020, **4**, 2741

Atomic scale insight into the fundamental mechanism of Mn doped $LiFePO_4$†

Fei Jiang,[a] Ke Qu,‡[bc] Mingshan Wang,*[a] Junchen Chen,[a] Yang Liu,[a] Hao Xu,[a] Yun Huang,[a] Jiangyu Li,*[b] Peng Gao,*[c] Jianming Zheng,[d] Mingyang Chen*[ef] and Xing Li*[a]

Received 26th February 2020
Accepted 31st March 2020

DOI: 10.1039/d0se00312c

rsc.li/sustainable-energy

A systematical and atomic scale investigation on the fundamental mechanism of Mn doped $LiFePO_4$ is conducted in this work. For the first time, it is found that the doping depth of Mn on the surface of $LiFePO_4$ is 10–15 nm. High-angle annular dark-field scanning transmission electron microscopy (HAADF-STEM) results further on the atomic scale demonstrate that Mn doping could effectively protect the crystal structure of $LiFePO_4$ from being corroded by the electrolyte during electrochemical cycling. Density functional theory (DFT) calculations suggest that the Mn doped $LiFePO_4$ could be regarded as a composite with $LiFePO_4$ bulk as the core and $LiMn_xFe_{1-x}PO_4$ as the outer layers. Unlike pure $LiFePO_4$, the Mn doped olivine $LiFePO_4$ ($LiMn_xFe_{1-x}PO_4$) is more stable and less susceptible to phase transition related amorphization, and thus could serve as a protective shell against $LiFePO_4$ degradation during electrochemical cycling.

1. Introduction

Olivine-type $LiFePO_4$ (LFP)[1] has been considered as a promising cathode material because of its low cost, superior thermal safety, high reversibility and acceptable operating voltage (3.45 *vs.* Li^+/Li).[2–6] The electrochemical lithiation–delithiation behavior of $LiFePO_4$ has been well understood in recent years through some *in situ* advanced characterization techniques, such as *operando* X-ray scattering methods.[7–15] However, for its large-scale application in electric vehicles (EVs), $LiFePO_4$ still faces two critical challenges, both of which may be viewed as kinetic and non-equilibrium in nature. One challenge is the fast charging problem.[16,17] It is well known that both electronic conductivity and ionic conductivity (Li-ion diffusion coefficient) are necessary.[18] However, $LiFePO_4$ exhibits low intrinsic electronic conductivity (10^{-9} S cm^{-1})[19] and a sluggish lithium ion diffusion coefficient (D_{Li^+}),[20–22] resulting in poor high-rate capability and poor cycling performance. The other key challenge for $LiFePO_4$ is its structural stability during electrochemical cycling. Although the strong P–O covalent bond structure in olivine-type $LiFePO_4$ could prohibit oxygen release, electrolyte aggressiveness and Fe dissolution upon extended cycling will seriously limit $LiFePO_4$ performance and ultimate utility.[23–27] Moreover, the dissolved Fe will migrate to the anode and catalytically destabilize the solid electrolyte interphase (SEI), leading to quick failure of the corresponding battery.[28–32]

In order to solve the abovementioned challenges, many strategies have been proposed to improve the electrochemical performances of $LiFePO_4$. They include coating the surface with conductive carbon[33–38] or other conductive materials, forming composites with graphene or carbon nanotubes,[39–42] controlling the particle sizes[43–47] and doping the surface with transition metal elements.[48–50] Mn doping has been recognized as an effective approach because a small amount of Mn doping could effectively improve the electrochemical performance of $LiFePO_4$.[51–54] However, few reports could clearly demonstrate the corresponding fundamental mechanisms. Actually, olivines structure lithium metal phosphates [$LiMPO_4$ (M = Fe, Mn, *et al.*)] also include another member of $LiMnPO_4$,[55,56] which could exhibit a higher Mn^{2+}/Mn^{3+} redox potential (4.1 V) in Li-ion batteries.[57–59] Unfortunately, the application of $LiMnPO_4$ is usually hindered by the Jahn–Teller distortion of Mn^{3+}

[a]*School of New Energy and Materials, Southwest Petroleum University, Chengdu, Sichuan 610500, China. E-mail: ustbwangmingshan@163.com; lixing@swpu.edu.cn*

[b]*Shenzhen Key Laboratory of Nanobiomechanics, Shenzhen Institutes of Advanced Technology, Chinese Academy of Sciences, Shenzhen 518055, China. E-mail: jy.li1@siat.ac.cn*

[c]*Electron Microscopy Laboratory, School of Physics, International Center for Quantum Materials, Peking University, Beijing, China. E-mail: p-gao@pku.edu.cn*

[d]*College of Chemistry and Chemical Engineering, Xiamen University, Xiamen 361005, China*

[e]*Center for Green Innovation, School of Materials Science and Engineering, University of Science and Technology Beijing, Beijing 100083, China. E-mail: mychen@ustb.edu.cn*

[f]*Beijing Computation Science Research Center, Beijing 100193, China*

† Electronic supplementary information (ESI) available. See DOI: 10.1039/d0se00312c

‡ Dr Ke Qu contributed equally to the first author.

during electrochemical cycling.[60,61] $LiMnPO_4$ is valued for its high charging and discharging platform, but its performance in other aspects is still inferior to that of $LiFePO_4$. Therefore, many researchers have focused on the advantages of $LiMnPO_4$ and $LiFePO_4$ to synthesize $LiMn_xFe_{1-x}PO_4$ ($0 \leqq x \leqq 1$).[50,62–69] Actually, Mn doped $LiFePO_4$ could be regarded as a composite with $LiFePO_4$ bulk as the core and $LiFe_xMn_{1-x}PO_4$ as the outer layer. In this study, aberration corrected high-angle annular dark-field scanning transmission electron microscopy (HAADF-STEM) imaging combined with Density Functional Theory (DFT) simulation, X-ray Photoelectron Spectroscopy (XPS) and electrochemical impedance spectroscopy (EIS) were employed to firstly provide a systematical and atomic scale investigation on the mechanism of Mn superficially doped $LiFePO_4$ for suppressing the capacity and voltage decay.

2. Experimental section

2.1 Material synthesis

$LiFePO_4$ (LFP) was purchased from Süd-Chemie Company. The Mn doped $LiFePO_4$ (Mn-LFP) was prepared through a wet chemical method. Firstly, manganese acetate (10^{-3} mol L^{-1}) and $LiFePO_4$ powder (0.5 g) were dispersed together in ethyl alcohol with constant stirring and ultrasonic treatment for 1 h. The solution was then slowly evaporated under vigorous stirring at 60 °C to obtain the dried mixture. Finally, it was sintered at 500 °C for 4 h in an argon atmosphere to obtain the Mn superficially doped $LiFePO_4$ sample. The content of Mn in the Mn doped $LiFePO_4$ was set as 0.1 wt%, 0.5 wt% and 1.0 wt%, respectively. The 0.5 wt% Mn doped $LiFePO_4$ exhibited the most stable cycling performance as shown in Fig. S1† and was selected as the focus of this study.

2.2 Microstructural characterization

Powder X-ray diffraction XRD (Panalytical X'pert MPD DY1219, Cu K_α radiation) was employed to characterize the crystal structure of pristine LFP and the as-prepared Mn-LFP. The macroscopic morphologies of pristine LFP and the as-prepared Mn-LFP were characterized by scanning electron microscopy (SEM, Hitachi SU8010). A probe-aberration-corrected FEI Titan 300 kV scanning transmission electron microscope (STEM) was employed for the high-angle annular dark-field (HAADF) analysis. With HAADF, the image intensity of each atomic column reflects the related average atomic number ($Z^{1.7}$). An FEI Talos 200X was employed for energy dispersive X-ray spectroscopy (EDS) mapping of the samples. The cross section of the sample was cut by using a Focused Ion Beam (FIB, Helios NanoLab 460HP). The cycled coin cells were disassembled in a high-purity argon filled glove box. The cycled $LiFePO_4$, Mn doped $LiFePO_4$ cathodes and the corresponding cycled Li metal anodes were thoroughly washed with pure DMC solvent to remove the residual electrolyte. In order to avoid the exposure to air atmosphere, the samples were kept in a glove box and transferred for TEM and XPS characterization within a sealed plastic bag. X-ray photoelectron spectroscopy (XPS, Phi 5000 Versaprobe iii) was conducted to analyze the formed cathode electrolyte interphase (CEI) compositions on the surfaces of cycled $LiFePO_4$ and Mn doped $LiFePO_4$ cathodes, and their corresponding formed solid electrolyte interphase (SEI) composites on the surfaces of cycled Li metal anodes. XPS was also employed to analyze the pristine LFP and Mn-LFP powder samples.

2.3 Electrochemical measurements

A slurry consisting of cathode active material ($LiFePO_4$ or Mn doped $LiFePO_4$), acetylene black (AB) and poly (vinylidene fluoride) (PVDF) binder at a weight ratio of 80 : 10 : 10 was well prepared. The slurry was cast onto an aluminum current collector with an active material loading of about 5 mg cm^{-2}. Then, it was cut into a disk of 1.4 cm in diameter, dried under vacuum at 60 °C for 12 h and used as the cathode. A Celgard 2500 separator is used as the cell separator and Li metal with a thickness of 250 μm is used as the anode. The electrolyte was 1.0 M $LiPF_6$ in EC : EMC (4 : 6 by vol.). The electrochemical performances were determined in standard CR2032 coin-type cells. The cells were assembled in an argon-filled glovebox with both water vapor and oxygen contents being less than 0.1 ppm. The electrochemical testing was performed using a BTS-5V20 mA galvanostatic testing instrument (NEWARE Electronic Co., Ltd) in the voltage range of 2.5–4.2 V *vs.* Li/Li^+. Electrochemical impedance spectroscopy (EIS) was performed in the charged state of 4.0 V in the frequency range of 10^5 to 10^{-2} Hz with a potential perturbation amplitude of 10 mV. The cyclic voltammetry (CV) curves were recorded between 2.5 and 4.2 V at different scan rates of 0.1, 0.2, 0.3, 0.5, 0.8 and 1 mV s^{-1}. An electrochemical workstation CH Instruments CHI760E was employed for the EIS and CV analyses.

2.4 Extended computational details

The pure and Mn doped olivine $FePO_4$ materials were modelled with a 2 × 3 × 1 supercell comprising 24 phosphate units; the pure and Mn doped α-quartz $FePO_4$ materials were modelled with a 4 × 2 × 1 supercell comprising 24 phosphate units. During the optimization of the supercell, both the lattice parameters and the atom positions were relaxed, until the energy and force convergence reach 10^{-5} eV and 0.01 eV $Å^{-1}$. The optimized lattice parameters are a = 9.812 Å, b = 17.929 Å, and c = 9.986 Å for the pure olivine $FePO_4$ supercell (space group: *Pnma*), and are a = 20.757 Å, b = 10.389 Å, and c = 11.514 Å for the pure α-quartz $FePO_4$ supercell (space group: $P3_121$).

All of the density functional theory (DFT)[70] calculations were performed using the Vienna *Ab Initio* Simulation Package (VASP)[71] with the projector-augmented-wave (PAW)[72] potentials. The structure optimization calculations were performed with the Perdew–Burke–Ernzerhof (PBE)[73] exchange-correlation functional. The energy cut-off was set to 500 eV for all of the calculations. A 4 × 2 × 4 and a 2 × 3 × 3 Monkhorst–Pack grid[74] were used to sample the Brillouin zone (BZ) of olivine and α-quartz structures, respectively.

3. Results and discussion

3.1 As-synthesized materials

Fig. S2† shows that there is no obvious difference between the SEM images of pristine LFP (a) and pristine Mn-LFP (b). However, the pristine Mn-LFP shows more agglomeration than the pristine LFP, which should be due to the annealing process for the Mn doping. Fig. 1(a) and (b) show the HAADF-STEM micrographs of the pristine LFP surface and bulk oriented along the [010] zone axis, where a good olivine crystal structure can be observed. Fig. 1(c) exhibits the atomic model of the olivine structure of LFP oriented along the [010] zone axis. The HAADF-STEM micrographs of the pristine Mn-LFP surface and bulk (Fig. 1(d) and (e)) oriented along the [010] zone axis also exhibit a good olivine crystal structure, which demonstrates that the Mn doping does not obviously affect the crystallinity. Fig. 1(f) shows the atomic model of the olivine structure of Mn-LFP oriented along the [010] zone axis. On the surface, some Mn occupies the Fe site, which vividly presents that Mn is doped into the surface of LFP. The HAADF-STEM micrograph of Mn-LFP (Fig. 1(g)) and the corresponding EDS mapping of Fe, P, Mn and O (Fig. 1(h)–(k)) show that there is uniform dispersion of Mn element on the surface of Mn-LFP, which demonstrates that the Mn element might be doped into the surface of LFP.

In order to further prove that Mn has been doped into the surface of LFP, XPS survey spectra were recorded for the pristine LFP and Mn-LFP powder samples as shown in Fig. S4.† There is no obvious difference between the high resolution XPS spectra of P 2p and Fe 2p in the comparison of pristine LFP (Fig. 2(a) and (b)) and pristine Mn-LFP (Fig. 2(d) and (e)). Fig. 2(c) and (f) present the high resolution XPS spectra of Mn 2p for $Mn(CH_3COO)_2$ and the doped Mn in the surface of LFP, respectively. It could be observed that the doped Mn 2p shows 0.3 eV higher binding energy than the Mn 2p for $Mn(CH_3COO)_2$, which should be ascribed to the stronger Mn–O bond for the doped Mn. Actually, the doped Mn 2p should be located in the chemical environmental of the MnO_6 octahedral crystal structure while the Mn 2p for $Mn(CH_3COO)_2$ being of Mn–O single bond chemical environment. Moreover, Fig. 2(g) shows the high resolution XPS spectra of Mn 2p for the doped Mn in the Mn-LFP surface at different depths of 0, 1, 2, 3, 5, 8 and 10 nm, where it could be observed that the intensity decreases with the increase of the depth. This further demonstrates that the Mn has been successfully doped into the surface of LFP. Furthermore, it also indicates that there is a limited depth for the Mn doping.

Fig. 3(a) and (b) present the SEM images of pristine Mn-LFP and the cross section of pristine Mn-LFP cut by using a Focused Ion Beam (FIB). The sample was fixed on conductive tape, and then was sent into the SEM cavity and adjusted to the right position for the FIB cutting. In order to maximize the ion beam damage, an ion beam of 30 kV (0.23 nA) was firstly employed to cut the Mn-LFP particle to obtain the cross section. Then, an ion beam of 5 kV (15 pA) was employed to clean up the damage (usually an amorphous layer). Finally, a 15 kV (0.8 nA) ion beam was employed to get the EDS line scanning data. From Fig. 3(c) and (d) showing the EDS line scanning of Fe and Mn, it could be observed that the doping depth for Mn in the surface of LFP is

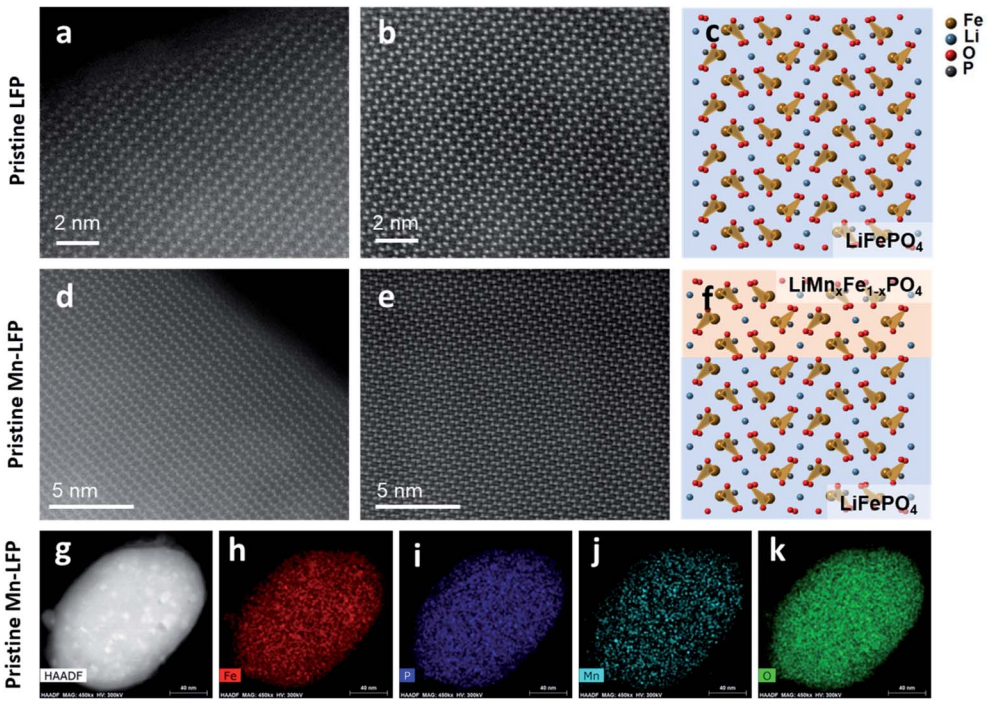

Fig. 1 (a) and (b) HAADF-STEM micrographs of the LFP surface and bulk, oriented along the [010] zone axis. (c) Atomic model of the olivine structure of LFP oriented along the [010] zone axis. (d)–(f) Analogous HAADF-STEM micrographs and atomic model for Mn doped LFP (Mn-LFP). (g)–(k) HAADF-STEM micrograph of Mn-LFP and the corresponding EDS mapping of Fe, P, Mn and O.

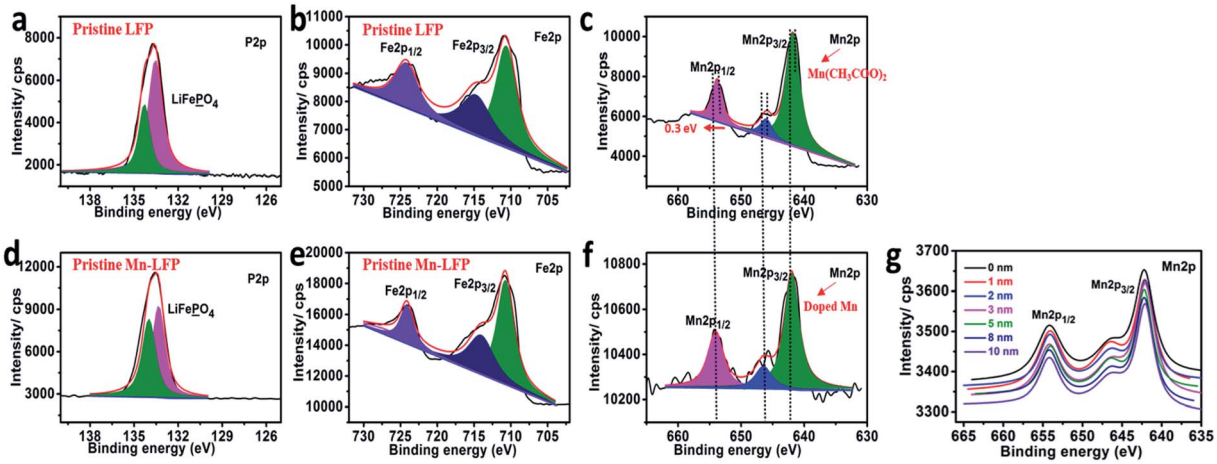

Fig. 2 (a) and (b) High resolution XPS spectra of P 2p and Fe 2p for pristine LFP (c) and Mn 2p for manganese acetate ($Mn(CH_3COO)_2$) in the precursor. (d) and (e) High resolution XPS spectra of P 2p and Fe 2p for pristine Mn-LFP, (f) Mn 2p for the doped Mn in the Mn-LFP surface, (g) and Mn 2p for the doped Mn in the Mn-LFP surface at different depths of 0, 1, 2, 3, 5, 8 and 10 nm.

10–15 nm. In fact, we also performed the EDS lining scanning on numerous particles, which confirmed a similar Mn doping depth on the surface of LFP. Fig. S3† shows the XRD patterns of pristine LFP and pristine Mn-LFP. The lattice parameters of *a*, *b* and *c* for pristine Mn-LFP are larger than those of pristine LFP, which should be attributed to the fact that the Mn^{2+} (0.83 Å) radius is larger than that of Fe^{2+} (0.63 Å). This also further proves that the Mn element has successfully doped into the surface of LFP.

3.2 Electrochemical performance

Fig. 4 shows the electrochemical performances of the LFP and Mn-LFP electrodes, respectively. Fig. 4(a) shows the long-term cycling performance of LFP and Mn-LFP at 1C, after 3 formation cycles at C/10. At a 1C rate, pristine LFP presents a discharge capacity of 145 mA h g^{-1}, and after cycling 500 times, the discharge capacity is 119 mA h g^{-1} with a capacity retention of 82%. In contrast, at a 1C rate, the Mn-LFP discharge capacity is 149 mA h g^{-1}, and after cycling 500 times, the discharge capacity is 139 mA h g^{-1} with a capacity retention of 93%. Furthermore, the first discharge capacity of LFP is 150 mA h g^{-1} at C/10, with a coulombic efficiency of 92%, which is much lower than 158 mA h g^{-1} of Mn-LFP with a coulombic efficiency of 94%. The improved cycling stability and initial coulombic efficiency of Mn-LFP indicate that Mn doping dramatically improves material surface stability. Fig. 4(b) and (c) show the charge/discharge profiles for LFP and Mn-LFP, tested for 500 cycles at 1C. It could be observed that the charge and discharge plateau gap under different cycles at 1C for LFP is obviously larger than that of Mn-LFP, which indicates that the LFP electrode presents more serious voltage degradation than Mn-LFP during the electrochemical cycling. Moreover, from the cycling performances of pristine LFP and Mn-LFP, it also could be observed that the CE and capacity degradation

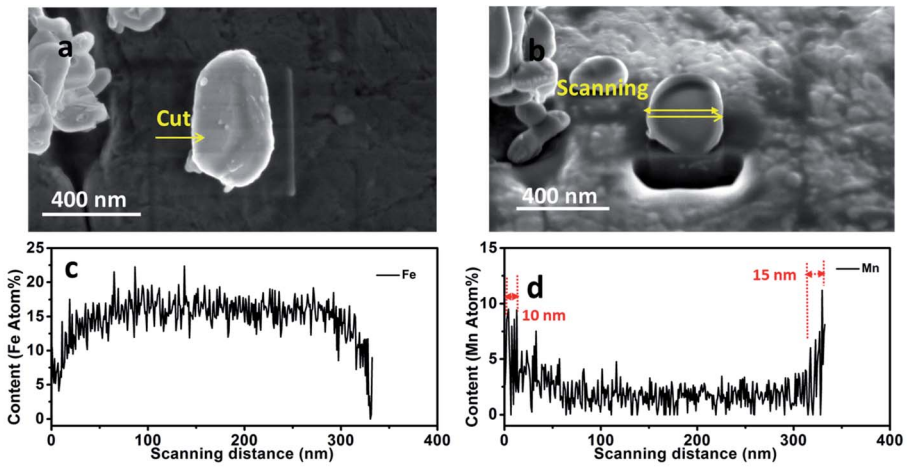

Fig. 3 (a) SEM image of pristine Mn-LFP. (b) SEM image of the cross section of pristine Mn-LFP cut by using a Focused Ion Beam (FIB). (c) and (d) EDS line scanning of Fe and Mn.

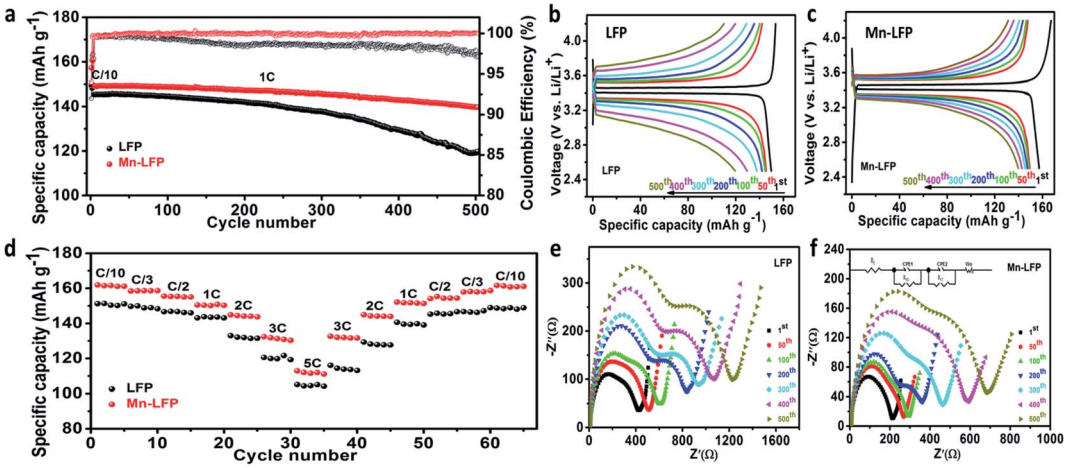

Fig. 4 (a) Cycling performance of LFP and Mn-LFP cycled at 1C, after 3 formation cycles at C/10. (b) and (c) Galvanostatic charge–discharge curves of pristine LFP and Mn-LFP, tested for 500 cycles at 1C (170 mA h g^{-1}) between 2.5 and 4.2 V *vs.* Li/Li^+. (d) Master plot showing the rate capability difference in pristine LFP *vs.* Mn-LFP. (e) and (f) Nyquist plots of LFP (e) and Mn-LFP (f) after the 1st, 50th, 100th, 200th, 300th, 400th and 500th cycles at a 1C rate, respectively. The impedance spectra were collected at the charged state of 4.0 V.

start in the ~80th cycle for pristine LFP, further deteriorating in the ~200th cycle, which indicates that the amorphorization effect starts to play a dominating role in the ~200th cycle (it will be further discussed in Fig. 5). In contrast, Mn-LFP does not show obvious CE and capacity degradation during the electrochemical cycling, which might demonstrate that there is no amorphorization effect.

Fig. 4(d) shows the rate capabilities of LFP and Mn-LFP electrodes tested from C/10 to 5C. It could be observed that the Mn-LFP cathode presents a higher discharge capacity of 161, 158, 155, 150, 144, 132, 112, 132, 144, 151, 154, 158 and 161 mA h g^{-1} at C/10, C/3, C/2, 1C, 2C, 3C, 5C, 3C, 2C, 1C, C/2, C/3, and C/10, respectively. As a comparison, the LFP cathode only presents 151, 148, 146, 143, 132, 120, 105, 114, 128, 139, 145, 146 and 148 mA h g^{-1} at the same current rates. Furthermore, Table 1 demonstrates that the electrochemical properties reported in this work also exhibit obvious advantages over previously published literature on Mn doped LFP. Fig. S5† exhibits the CV curves of the LFP and Mn-LFP cathodes at different scan rates of 0.1, 0.2, 0.3, 0.5, 0.8 to 1 mV s^{-1}. With the scan rate increasing, the potential difference between the cathodic and anodic peaks for both of the cathodes becomes large. However, LFP shows larger cathodic and anodic potential differences of 0.32, 0.44, 0.53, 0.70, 0.88 and 0.98 V at different scan rates than

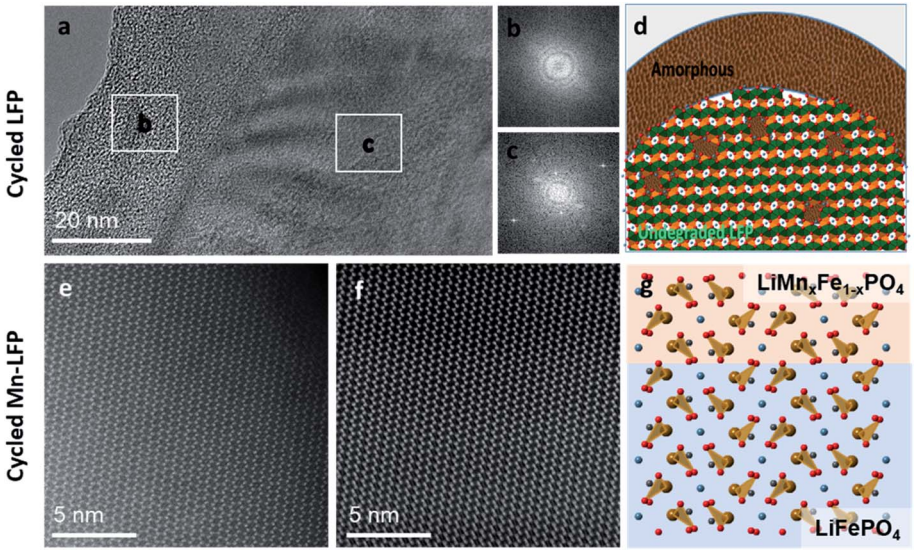

Fig. 5 (a) HRTEM image of cycled LFP after 500 cycles at 1C, with regions near-surface (b) and bulk (c) identified by rectangles. (d) Schematic model of cycled LFP where the surface is amorphous; meanwhile there are also amorphous regions in the bulk. (e)–(g) HAADF-STEM images of cycled Mn-LFP near-surface and bulk oriented along the [010] zone axis. (f) Atomic model of the olivine structure of cycled Mn-LFP oriented along the [010] zone axis.

Table 1 The electrochemical performance comparisons with previously published literature on Mn doped $LiFePO_4$

0.1C (mA h g^{-1})	0.5C (mA h g^{-1})	1C (mA h g^{-1})	2C (mA h g^{-1})	5C (mA h g^{-1})	
161.0	155.0	150.0	144.0	112.0	This work
156.0	—	—	—	110.0	54
—	152.0	131.0	105.0	—	65
—	142.5	130.5	115.0	96.3	52
155.0	139.0	130.0	115.0	87.0	53
128.0	—	109.0	—	—	66
121.0	—	—	110.0	91.0	64
—	—	—	—	107.0	57
136.6	117.0	—	—	—	68
—	150.0	—	121.0	—	69
145.0	134.0	119.0	—	97.0	67

Mn-LFP of 0.31, 0.36, 0.40, 0.62, 0.75 and 0.81 V. This further demonstrates that the Mn-LFP cathode shows better rate capability than the LFP cathode.

Fig. 4(e) and (f) show the electrochemical impedance spectroscopy (EIS) spectra of the LFP and Mn-LFP electrodes after the 1st, 50th, 100th, 200th, 300th, 400th and 500th cycles, respectively. The Nyquist plots contain a semicircle located in the high frequency region, which correlates with the surface film resistance R_{CEI} and is associated with the CEI/SEI layer.[75,76] A second semicircle located in a lower frequency region represents the charge transfer resistance (R_{CT}), being correlated with the reaction control resistance of the primary active material.[77,78] An oblique line located in the low frequency region represents the Warburg impedance (W), being associated with ion diffusion limitations in the electrode.[79] The intercept at high frequency with the real axis is associated with electrolyte resistance (R_E).[80,81] The lithium ion diffusion coefficient (D_{Li^+}) of LFP and Mn-LFP in the cycles of 1–500 is calculated from the Warburg impedance coefficient (σ_W) using eqn (1) and (2),[82,83]

$$Z_{re} = (R_{sf} + R_{CT} + \sigma_W \omega^{-1/2}) \quad (1)$$

$$D_{Li^+} = R^2T^2/(2A^2n^4F^4C^2\sigma_W{}^2) \quad (2)$$

where D_{Li^+} represents the rate limiting lithium ion diffusion coefficient. R is the gas constant, T is the absolute temperature, A is the effective area of the electrode, n is the number of electrons transferred, F is the Faraday constant, and C is the concentration of lithium ions. The Warburg impedance coefficient σ_W could be determined from the slope of Z_{re} as a function of $\omega^{-1/2}$, as shown in Fig. S6.†

Table 2 shows fitted parameters and calculated D_{Li^+} for the experimental EIS spectra of LFP and Mn-LFP electrodes. For the LFP electrode, the R_{CEI} and R_{CT} values are 216.2, 224.8, 285.6, 434.7, 510.2, 555.4, and 628.6 ohm and 182.1, 246.4, 263.1, 377.0, 434.8, 474.7, and 563.3 ohm in the 1st, 50th, 100th, 200th, 300th, 400th and 500th cycles, respectively. The corresponding R_{CEI} and R_{CT} values for Mn-LFP are obviously lower, being 126.3, 175.9, 183.5, 215.9, 258.2, 271.9, and 338.3 ohm and 74.9, 84.2, 101.1, 142.1, 190.3, 292.0, and 319.6 ohm, respectively. The R_E for the LFP electrode is also obviously larger than that of the Mn-LFP electrode in the 1st, 50th, 100th, 200th, 300th, 400th and 500th cycles as shown in Table 1. Moreover, the D_{Li^+} for the LFP electrode from the 1st cycle of 3.85×10^{-10} cm^2 s^{-1} quickly degrades to 2.34×10^{-11} cm^2 s^{-1} in the 500th cycle. However, the D_{Li^+} for the Mn-LFP electrode at the same stage only drops from 1.98×10^{-9} cm^2 s^{-1} to 1.14×10^{-10} cm^2 s^{-1}. The quick polarization increase of R_E, R_{CEI}, R_{SEI} and D_{Li^+} degradation for the LFP electrode demonstrates that it might experience serious electrode corrosion by the electrolyte during the electrochemical cycling. For the Mn-LFP electrode, however, the electrode corrosion is effectively suppressed during the electrochemical cycling, which should be due to the fact that the Mn doping could stabilize the surface of LFP.

3.3 Cycled cathode–electrolyte interface

Cycling induced structural evolution was characterized at the atomic scale by employing HRTEM and HAADF-STEM. Fig. 5(a) shows the HRTEM image of LFP after 500 cycles at a 1C rate. From the Fast Fourier Transformation (FFT) as shown in Fig. 5(b) and (c) corresponding to the rectangles in the surface and bulk of LFP as shown in Fig. 5(a), it is evident that the outer layer of cycled LFP has been fully amorphized. Meanwhile, the bulk also shows regions of amorphization. This is illustrated in the schematic panel of Fig. 5(d). The atomic resolution HAADF-STEM images of the cycled LFP could not be obtained due to its extensive disorder. The growth of the amorphized regions is correlated with a significant decline of D_{Li^+}, which well explains why LFP shows quick degradation of D_{Li^+} during the

Table 2 Fitted parameters and calculated D_{Li^+} for the experimental EIS spectra of LFP and Mn-LFP electrodes and those calculated using an equivalent circuit as shown in the inset of Fig. 4(f)

	LFP pristine				Mn-LFP			
Cycle number	R_E/ohm	R_{CEI}/ohm	R_{CT}/ohm	D_{Li^+} (cm^2 s^{-1})	R_E/ohm	R_{CEI}/ohm	R_{CT}/ohm	D_{Li^+} (cm^2 s^{-1})
1st	3.5	216.2	182.1	3.85×10^{-10}	3.4	126.3	74.9	1.98×10^{-9}
50th	3.8	224.8	246.4	1.49×10^{-10}	3.6	175.9	84.2	6.12×10^{-10}
100th	4.2	285.6	263.1	1.25×10^{-10}	3.7	183.5	101.1	5.76×10^{-10}
200th	4.3	434.7	377.0	4.45×10^{-11}	4.1	215.9	142.1	2.20×10^{-10}
300th	4.7	510.2	434.8	3.90×10^{-11}	4.5	258.2	190.3	2.10×10^{-10}
400th	5.3	555.4	474.7	2.61×10^{-11}	4.8	271.9	292.0	2.09×10^{-10}
500th	5.5	628.6	563.3	2.34×10^{-11}	5.0	338.3	319.6	1.14×10^{-10}

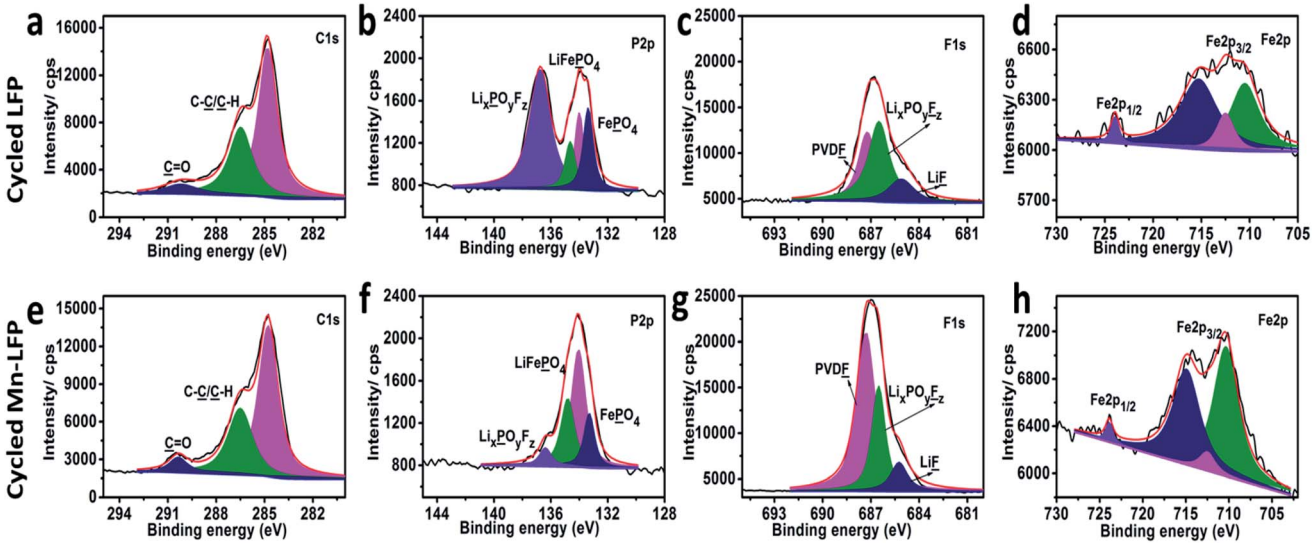

Fig. 6 (a)–(d) High resolution XPS spectra of C 1s, P 2p, F 1s and Fe 2p for cycled LFP. (e)–(h) High resolution XPS spectra of C 1s, P 2p, F 1s and Fe 2p for cycled Mn-LFP.

electrochemical cycling. The HAADF-STEM images of the cycled Mn-LFP near-surface and bulk oriented along the [010] zone axis are shown in Fig. 5(e) and (f). The atomic model of the olivine structure of cycled Mn-LFP oriented along the [010] zone axis is shown in Fig. 5(g). It could be observed that Mn-LFP still retains its good olivine crystal structure although experiencing 500 cycles at 1C, which further proves that the Mn doping could stabilize the surface of LFP. After a long cycle, it can be seen that the outer crystal structure of LFP is destroyed, while the crystal structure of Mn-LFP is still intact and in Fig. S7(g)† manganese is still evenly distributed, which further indicates that the doped manganese shell can improve the stability of the material.

Fig. 6 and S8† compare the survey and high resolution XPS spectra of the LFP and Mn-LFP cathodes after 500 cycles at a 1C rate. The spectrum shows peak splitting for Fe $2p_{1/2}$ (724.3 eV) and Fe $2p_{3/2}$ (710.5 eV) and a satellite peak of Fe $2p_{3/2}$ (715.5 eV) as shown in Fig. 6(d)–(h) which belong to $LiFePO_4$.[49] It needs to be noted that there is an Fe $2p_{3/2}$ peak located at 712.5 eV which belongs to $FePO_4$ for both of the cycled LFP and Mn-LFP. This further demonstrates that some Fe^{2+} is transformed into Fe^{3+} during the electrochemical cycling, which is known to be inactive.[84,85] However, the cycled Mn-LFP displays a lower relative intensity of Fe^{3+} as compared with the cycled LFP. This indicates that more Fe^{2+} is preserved in the outer surface of LFP due to the Mn doping. These results well explain why Mn-LFP exhibits better electrochemical performances and maintains a good olivine structure during the electrochemical cycling. Moreover, the peak intensity of the P 2p spectrum ($Li_xPO_yF_z$) for

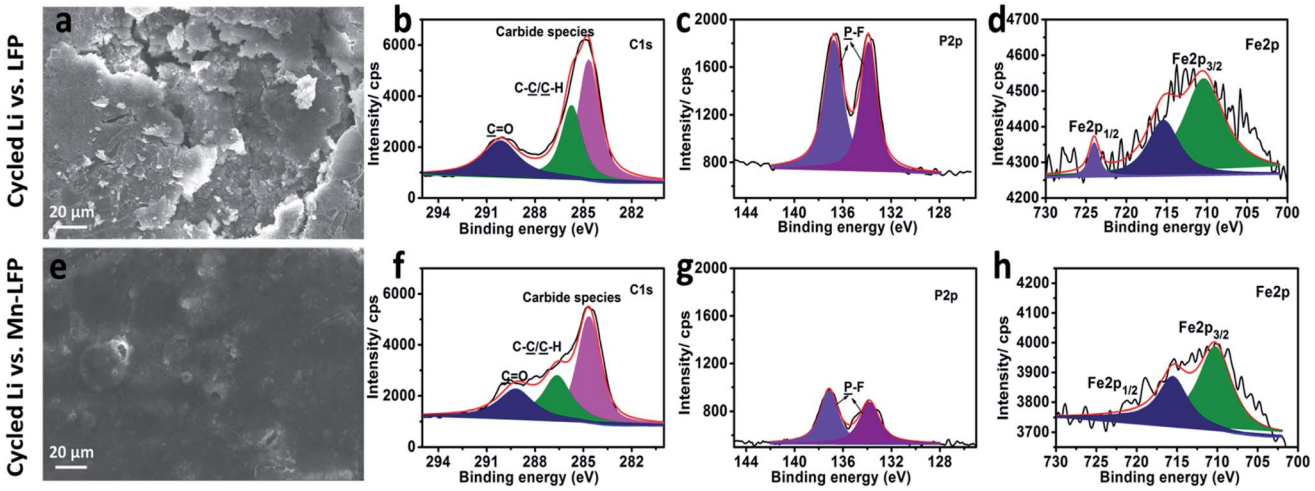

Fig. 7 SEM top view images of post 500 cycled Li metal anode surfaces (a) and (e) the XPS high resolution spectra analysis of C 1s, P 2p and Fe 2p corresponding to the SEI chemistry formed on the cycled Li metal anodes. Panels (b)–(d) show the anode tested against LFP; panels (f)–(h) show the anode tested against Mn-LFP.

the cycled LFP (Fig. 6(b)) is also obviously stronger than that of the cycled Mn-LFP (Fig. 6(f)), which indicates that more cathode electrolyte interphase (CEI) might be formed during the electrochemical cycling. The thicker CEI could result in large electrode polarization, which well explains why the LFP electrode exhibits larger resistance than Mn-LFP.

3.4 Cycled anode electrolyte interface

Fig. 7(a) and (e) show the SEM top view images of post 500 cycled Li metal anode surfaces tested against LFP and Mn-LFP, respectively. It could be observed that there is a cracked solid electrolyte interphase (SEI) formed on the cycled Li anode tested against LFP while a smooth SEI for that tested against Mn-LFP. Fig. S9† shows the comparison of XPS survey spectra of the formed SEI on the cycled Li metal anode tested against LFP and Mn-LFP. Fig. 7(b)–(d) and (f)–(h) present the high resolution XPS spectra of C 1s, P 2p and Fe 2p for the corresponding SEI compositions on Li *vs.* LFP and Li *vs.* Mn-LFP, respectively. The high resolution XPS spectra of F 1s and O 1s for both are shown in Fig. S10.† For both of LFP and Mn-LFP, the anode SEI films contain the same components of $Li_xPF_yO_z$ (685.4 eV) and LiF (683.5 eV) in F 1s, the P–F composite (133–137 eV) in P 2p, the carbonyl group (288.7 eV (C=O)), carbon and hydrocarbon (285.0 eV (C–C/C–H)) and carbide species (283.0–283.5 eV) in C 1s spectra, and the carbonyl (530.5 eV (C=O))/ether oxygen (532.0 eV –$(CH_2–CH_2–O)_n$–) in O 1s spectra. These species agree with prior analysis of SEI species on Li metal anodes.[80] However, the relative intensity of C 1s, P 2p, F 1s and O 1s for that *vs.* LFP is stronger than that *vs.* Mn-LFP. This demonstrates that there might be a thicker SEI formed on the Li anode *vs.* LFP than *vs.* Mn-LFP. The cracked and thicker SEI could also result in larger electrode resistance. The relative peak intensity of Fe 2p within the SEI layer when tested against Mn-LFP is significantly lower than when tested against LFP. Furthermore, from the EDS mapping as shown in Fig. S11,† it could be observed that the amount of Fe on Li *vs.* Mn-LFP is less than that on Li *vs.* LFP. This gives further direct evidence that the Mn doping reduces Fe dissolution during the electrochemical cycling, which should also be due to the fact that the Mn doping stabilizes the surface of LFP.

3.5 DFT modelling

To further understand the stabilization mechanism of Mn doping for LFP, DFT calculations were carried out, and the results are shown in Fig. 8. The fully delithiated LFPs ($FePO_4$) with and without Mn doping were modelled to understand the materials' stability upon severe depletion of lithium. Two phases of $FePO_4$, olivine and α-quartz, were considered. The olivine $FePO_4$ is the direct delithiation product of $LiFePO_4$ without a phase change, whereas the α-quartz phase is the thermally favourable phase for $FePO_4$. Note that the α-quartz $FePO_4$ lacks a good Li^+ diffusion channel as found in olivine LFP and $FePO_4$; therefore, the phase transition from olivine to α-quartz (or amorphization towards α-quartz) will be detrimental to the Li^+

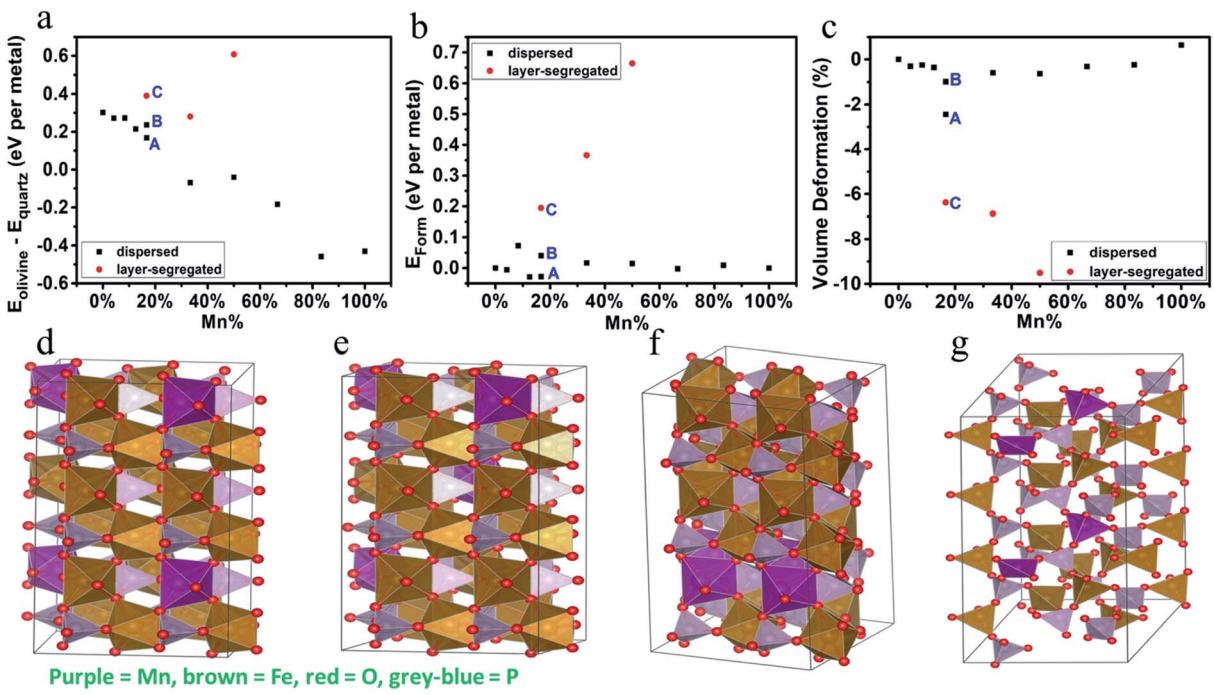

Fig. 8 (a) Predicted energy difference between olivine and α-quartz $FePO_4$ at different Mn concentrations at the DFT level. (b) Predicted formation energy E_{Form} for forming $Mn_xFe_{1-x}PO_4$ from pure $MnPO_4$ and $FePO_4$. (c) Volume deformation of $Mn_xFe_{1-x}PO_4$ with respect to pure $FePO_4$. In (a), (b), and (c), the letters A, B, and C label three olivine $Mn_{1/6}Fe_{5/6}PO_4$ homotops whose structures are shown in (d), (e), and (f), respectively. (d) Maximally dispersed olivine $Mn_{1/6}Fe_{5/6}PO_4$ homotop A, with a $Pmc2_1$ space group. (e) Low-symmetry dispersed olivine $Mn_{1/6}Fe_{5/6}PO_4$ homotop B, with a $P1$ space group. (f) Layer-segregated olivine $Mn_{1/6}Fe_{5/6}PO_4$ homotop C, with a $Pmc2_1$ space group. (g) The maximally dispersed α-quartz $Mn_{1/6}Fe_{5/6}PO_4$ homotop.

diffusion, which in turn undermines the battery performance. Here our results show, at an extremely low local Li concentration, that the olivine structure can possibly undergo a phase transition to form the α-quartz structure, and the introduction of an Mn-dopant can suppress such transitions.

First, the energy differences between the isomeric olivine and α-quartz $LiPO_4$ structures are predicted using eqn (3) (Fig. 8(a)).

$$\Delta E = E(\text{olivine}) - E(\alpha\text{-quartz}) \quad (3)$$

For pure $LiPO_4$, the α-quartz phase is 0.3 eV per phosphate more stable than the olivine phase, which implies a tendency for phase transition (Fig. 8 (a)). The Mn doping of $LiPO_4$ is modelled by replacing Fe atoms in the $LiPO_4$ supercells. As the Mn concentration increases, the olivine phase gains thermal favourability against the quartz phase (Fig. 8(a)). Once Fe atoms are fully replaced by Mn atoms, the olivine phase (*i.e.* pure olivine $MnPO_4$) becomes 0.4 eV per phosphate more stable than the α-quartz phase. This suggests that Mn doping can suppress the phase change. In addition, the formation energy E_{Form} for forming $Mn_xFe_{1-x}PO_4$ from pure $MnPO_4$ and $FePO_4$ is predicted using eqn (4)

$$E_{\text{Form}} = E(Mn_xFe_{1-x}PO_4) - xE(MnPO_4) - (1 - x)E(FePO_4) \quad (4)$$

where x is the Mn doping concentration for the doped $FePO_4$. The results (Fig. 8(b)) show that the Mn doping of $FePO_4$ is essentially thermally neutral, which implies that a fairly high local concentration of Mn can be achieved practically for the Mn doping of $FePO_4$.

From the experimental results, we learn that there exists an optimal Mn concentration that maximally enhances the electrochemical stability of LFP. Therefore, too high a Mn concentration might be detrimental to the stability of the doped LFP material. This seems to contradict the trend found by the predicted energy difference between the olivine and α-quartz phases where the favourability of olivine $FePO_4$ scales monotonically with the Mn concentration. So, there must be some other causes which lower the material's stability at a high Mn concentration. One consequence of increasing the doping concentration is that the number of homotops (isomeric structures with the same phase but with different ion position permutations) will be increased exponentially. The homotops can exhibit different stability despite belonging to the same mineral phase. The geometries and energy quantities were predicted for several typical homotops for the Mn doped olivine $FePO_4$. At a low Mn concentration (≤12.5%, with less than 4 Mn atoms in a supercell of 24 phosphates), the stability of homotops is approximately invariant to the Mn positions, as long as Mn is dispersed; this is only true for small supercells. Meanwhile, the cell parameters of these Mn doped olivine $FePO_4$ are close to those of pure $FePO_4$. At a Mn concentration of ~16.7% with 4 Mn atoms in the 24-phosphate supercell, the maximally dispersed olivine $Mn_{1/6}Fe_{5/6}PO_4$ homotop (with a $Pmc2_1$ space group, Fig. 8(d)) is ~0.1 eV per phosphate more stable than the low-symmetry dispersed homotop (with a $P1$ space group, Fig. 8(e)) and is ~0.2 eV per phosphate more stable than the layer-segregated homotop (with a $Pmc2_1$ space group, Fig. 8(f)). Note that the layer-segregated homotops that contain pure $MnPO_4$ layers are much less stable than the dispersed homotopes for all Mn concentrations, so they are quite unlikely to exist. Interestingly, the maximally dispersed $Mn_{1/6}Fe_{5/6}PO_4$ homotop has smaller lattice parameters than pure $FePO_4$, with a volume deformation of nearly 3%, which is not found at lower Mn concentration. Such mismatches may cause a stacking fault and dislocation or induce reconstruction of the interfacial structures, which could possibly block the Li^+ diffusion channels.

We can relate our computational results to the physical picture of the experiment. Upon rapid delithiation (*e.g.* during fast charging), the surface of LFP may be heavily delithiated as compared to the interior. Locally, the olivine $FePO_4$ structure could be formed in the surface region. The thermally favored olivine-to-quartz phase transition may occur, to some extent, causing the degradation of LFP. The Mn doped $LiFePO_4$ could be regarded as a composite with $LiFePO_4$ bulk as the core and $LiMn_xFe_{1-x}PO_4$ as the outer layers. The Mn concentration is likely to be high at the outermost layers and decreases with the depth into the material. When severe delithiation occurs, the outer layers of the composite may form delithiated local structures such as Mn doped $FePO_4$. Unlike pure $FePO_4$, the Mn doped olivine $FePO_4$ is less susceptible to phase transition or phase transition related amorphization, especially at high Mn concentrations, and thus can serve as a protective shell against LFP degradation during electrochemical cycling. It is also noted that an appropriately high Mn doping concentration could be the key for LFP stabilization. If the Mn concentration was too high, doped phosphates with comparatively small lattice parameters might be locally formed during delithiation to cause unfavorable structural changes and lower the battery performance.

4. Conclusion

The fundamental mechanisms of Mn doping improving the electrochemical performance of $LiFePO_4$ was systematically investigated in this work. For the first time, it is found that the Mn element could be doped into the surface of $LiFePO_4$ and the doping depth of Mn on the surface of $LiFePO_4$ is determined to be 10–15 nm through employing XPS, FIB and EDS mapping characterization. At a 1C rate, the Mn doped $LiFePO_4$ presents a discharge capacity of 149 mA h g^{-1}, and after 500 cycles, the discharge capacity is 139 mA h g^{-1} with a capacity retention of 93%. In contrast, pristine $LiFePO_4$ shows a discharge capacity of 145 mA h g^{-1} at a 1C rate, and only a discharge capacity of 119 mA h g^{-1} is maintained after 500 cycles with a capacity retention of 82%. Moreover, the Mn doped $LiFePO_4$ also exhibits obviously better rate capability than the pristine $LiFePO_4$. HAADF-STEM further demonstrates at the atomic scale that Mn doping could effectively suppress the degradation of the crystal structure of $LiFePO_4$ to an amorphous phase during electrochemical cycling. DFT calculations indicate that Mn doping could form a more stable $LiMn_xFe_{1-x}PO_4$ protective

shell, which could well protect $LiFePO_4$ from being corroded by the electrolyte during electrochemical cycling. The mechanism proposed in this work might also be applicable to the synthesis of Mn doped $LiFePO_4$ by other methods, which would advance the designing of cathode materials.

Conflicts of interest

There are no conflicts to declare.

Acknowledgements

This work was supported by the National Natural Science Foundation of China (grant no. 51502250 and U1930402) and the Science & Technology Department of Sichuan Province (grant no. 2019-GH02-00052-HZ, 2017JQ0044, and 2019YFG0220). The computational work was supported by the TH2-JK program at the Beijing Computational Science Research Center.

References

1 A. K. Padhi, K. S. Nanjundaswamy and J. B. Goodenough, *J. Electrochem. Soc.*, 1997, **144**, 1188–1194.
2 D. Li and H. Zhou, *Mater. Today*, 2014, **17**, 451–463.
3 J. B. Goodenough and K.-S. Park, *J. Am. Chem. Soc.*, 2013, **135**, 1167–1176.
4 L.-X. Yuan, Z.-H. Wang, W.-X. Zhang, X.-L. Hu, J.-T. Chen, Y.-H. Huang and J. B. Goodenough, *Energy Environ. Sci.*, 2011, **4**, 269–284.
5 Y. Wang, P. He and H. Zhou, *Energy Environ. Sci.*, 2011, **4**, 805–817.
6 N. Ravet, Y. Chouinard, J. F. Magnan, S. Besner, M. Gauthier and M. Armand, *J. Power Sources*, 2001, **97–98**, 503–507.
7 Y. Li, H. Chen, K. Lim, H. D. Deng, J. Lim, D. Fraggedakis, P. M. Attia, S. C. Lee, N. Jin, J. Moškon, Z. Guan, W. E. Gent, J. Hong, Y.-S. Yu, M. Gaberščček, M. Saiful Islam, M. Z. Bazant and W. C. Chueh, *Nat. Mater.*, 2018, **17**, 915–922.
8 J. Wang, Y.-c. K. Chen-Wiegart and J. Wang, *Nat. Commun.*, 2014, **5**, 4570.
9 J. Lim, Y. Li, D. H. Alsem, H. So, S. C. Lee, P. Bai, D. A. Cogswell, X. Liu, N. Jin, Y.-S. Yu, N. J. Salmon, D. A. Shapiro, M. Z. Bazant, T. Tyliszczak and W. C. Chueh, *Science*, 2016, **353**, 566–571.
10 L. Mu, Q. Yuan, C. Tian, C. Wei, K. Zhang, J. Liu, P. Pianetta, M. M. Doeff, Y. Liu and F. Lin, *Nat. Commun.*, 2018, **9**, 2810.
11 Y. Li, J. N. Weker, W. E. Gent, D. N. Mueller, J. Lim, D. A. Cogswell, T. Tyliszczak and W. C. Chueh, *Adv. Funct. Mater.*, 2015, **25**, 3677–3687.
12 N. Ohmer, B. Fenk, D. Samuelis, C.-C. Chen, J. Maier, M. Weigand, E. Goering and G. Schütz, *Nat. Commun.*, 2015, **6**, 6045.
13 L. Li, Y.-c. K. Chen-Wiegart, J. Wang, P. Gao, Q. Ding, Y.-S. Yu, F. Wang, J. Cabana, J. Wang and S. Jin, *Nat. Commun.*, 2015, **6**, 6883.
14 L. Hong, L. Li, Y. K. Chen-Wiegart, J. Wang, K. Xiang, L. Gan, W. Li, F. Meng, F. Wang, J. Wang, Y. M. Chiang, S. Jin and M. Tang, *Nat. Commun.*, 2017, **8**, 114.
15 J. Lu, T. Wu and K. Amine, *Nat. Energy*, 2017, **2**, 17011.
16 K. Zaghib, M. Dontigny, A. Guerfi, P. Charest, I. Rodrigues, A. Mauger and C. M. Julien, *J. Power Sources*, 2011, **196**, 3949–3954.
17 B. Kang and G. Ceder, *Nature*, 2009, **458**, 190–193.
18 J. Wang and X. Sun, *Energy Environ. Sci.*, 2015, **8**, 1110–1138.
19 R. Malik, D. Burch, M. Bazant and G. Ceder, *Nano Lett.*, 2010, **10**, 4123–4127.
20 D. Morgan, A. V. D. Ven and G. Ceder, *Electrochem. Solid-State Lett.*, 2004, **7**, A30–A32.
21 L. Laffont, C. Delacourt, P. Gibot, M. Y. Wu, P. Kooyman, C. Masquelier and J. M. Tarascon, *Chem. Mater.*, 2006, **18**, 5520–5529.
22 L. Yang, X. Zhu, X. Li, X. Zhao, K. Pei, W. You, X. Li, Y. Chen, C. Lin and R. Che, *Adv. Energy Mater.*, 2019, **9**, 1902174.
23 J. Wang, J. Yang, Y. Tang, R. Li, G. Liang, T. K. Sham and X. Sun, *J. Mater. Chem. A*, 2013, **1**, 1579–1586.
24 A. Mauger and C. Julien, *Ionics*, 2014, **20**, 751–787.
25 Y. Zhang, C.-Y. Wang and X. Tang, *J. Power Sources*, 2011, **196**, 1513–1520.
26 C. M. Julien, A. Mauger and K. Zaghib, *J. Mater. Chem.*, 2011, **21**, 9955–9968.
27 L. Castro, R. Dedryvère, J.-B. Ledeuil, J. Bréger, C. Tessier and D. Gonbeau, *J. Electrochem. Soc.*, 2012, **159**, A357–A363.
28 K. Amine, J. Liu and I. Belharouak, *Electrochem. Commun.*, 2005, **7**, 669–673.
29 K. Amine, J. Liu, S. Kang, I. Belharouak, Y. Hyung, D. Vissers and G. Henriksen, *J. Power Sources*, 2004, **129**, 14–19.
30 G.-M. Song, Y. Wu, Q. Xu and G. Liu, *J. Power Sources*, 2010, **195**, 3913–3917.
31 K. Striebel, A. Guerfi, J. Shim, M. Armand, M. Gauthier and K. Zaghib, *J. Power Sources*, 2003, **119–121**, 951–954.
32 K. Zaghib, N. Ravet, M. Gauthier, F. Gendron, A. Mauger, J. B. Goodenough and C. M. Julien, *J. Power Sources*, 2006, **163**, 560–566.
33 K. Zaghib, A. Mauger, F. Gendron and C. M. Julien, *Chem. Mater.*, 2008, **20**, 462–469.
34 Y. Wang, Y. Wang, E. Hosono, K. Wang and H. Zhou, *Angew. Chem.*, 2008, **120**, 7571–7575.
35 Y. Liu, J. Wang, J. Liu, M. N. Banis, B. Xiao, A. Lushington, W. Xiao, R. Li, T. K. Sham, G. Liang and X. Sun, *Nano Energy*, 2018, **45**, 52–60.
36 Y. Liu, J. Liu, J. Wang, M. N. Banis, B. Xiao, A. Lushington, W. Xiao, R. Li, T. K. Sham, G. Liang and X. Sun, *Nat. Commun.*, 2018, **9**, 929.
37 W. Wei, W. Lv, M.-B. Wu, F.-Y. Su, Y.-B. He, B. Li, F. Kang and Q. Yang, *Carbon*, 2013, **57**, 530–536.
38 M. Chen, C. Du, B. Song, K. Xiong, G. Yin, P. Zuo and X. Cheng, *J. Power Sources*, 2013, **223**, 100–106.
39 J. Wang and X. Sun, *Energy Environ. Sci.*, 2012, **5**, 5163–5185.
40 Z. Bakenov and I. Taniguchi, *J. Power Sources*, 2010, **195**, 7445–7451.
41 B. Wang, T. Liu, A. Liu, G. Liu, L. Wang, T. Gao, D. Wang and X. Zhao, *Adv. Energy Mater.*, 2016, **6**, 1600426.

42 A. K. Budumuru, M. Viji, A. Jena, B. R. K. Nanda and C. Sudakar, *J. Power Sources*, 2018, **406**, 50–62.
43 Z. Ma, G. Shao, Y. Fan, G. Wang, J. Song and T. Liu, *ACS Appl. Mater. Interfaces*, 2014, **6**, 9236–9244.
44 T. Liu, Y. Feng, Y. Duan, S. Cui, L. Lin, J. Hu, H. Guo, Z. Zhuo, J. Zheng, Y. Lin, W. Yang, K. Amine and F. Pan, *Nano Energy*, 2015, **18**, 187–195.
45 L. Wang, X. He, W. Sun, J. Wang, Y. Li and S. Fan, *Nano Lett.*, 2012, **12**, 5632–5636.
46 Z. Li, Z. Peng, H. Zhang, T. Hu, M. Hu, K. Zhu and X. Wang, *Nano Lett.*, 2016, **16**, 795–799.
47 B. Wang, Y. Xie, T. Liu, H. Luo, B. Wang, C. Wang, L. Wang, D. L. Wang, S. Dou and Y. Zhou, *Nano Energy*, 2017, **42**, 363–372.
48 A. Paolella, S. Turner, G. Bertoni, P. Hovington, R. Flacau, C. Boyer, Z. Feng, M. Colombo, S. Marras, M. Prato, L. Manna, A. Guerfi, G. P. Demopoulos, M. Armand and K. Zaghib, *Nano Lett.*, 2016, **16**, 2692–2697.
49 J. Tu, K. Wu, H. Tang, H. Zhou and S. Jiao, *J. Mater. Chem. A*, 2017, **5**, 17021–17028.
50 A. Paolella, G. Bertoni, E. Dilena, S. Marras, A. Ansaldo, L. Manna and C. George, *Nano Lett.*, 2014, **14**, 1477–1483.
51 H. Lee, S. Kim, N. S. Parmar, J.-H. Song, K.-y. Chung, K.-B. Kim and J.-W. Choi, *J. Power Sources*, 2019, **434**, 226713.
52 Y. Wang, Z.-S. Feng, L.-L. Wang, L. Yu, J.-J. Chen, Z. Liang and R. Wang, *RSC Adv.*, 2014, **4**, 51609.
53 L. T. N. Huynh, P. P. N. Le, V. D. Trinh, H. H. Tran, V. M. Tran and M. L. P. Le, *J. Chem.*, 2019, **2019**, 1–10.
54 Y. Liu, Y.-J. Gu, J.-L. Deng, G.-Y. Luo, F.-Z. Wu, Y. Mai, X.-Y. Dai and J.-Q. Li, *J. Mater. Sci.: Mater. Electron.*, 2019, **31**, 2887–2894.
55 T. Ruan, B. Wang, F. Wang, R. Song, F. Jin, Y. Zhou, D. Wang and S. Dou, *Nanoscale*, 2019, **11**, 3933–3944.
56 Y. Deng, C. Yang, K. Zou, X. Qin, Z. Zhao and G. Chen, *Adv. Energy Mater.*, 2017, **7**, 1601958.
57 B. Ding, P. Xiao, G. Ji, Y. Ma, L. Lu and J. Y. Lee, *ACS Appl. Mater. Interfaces*, 2013, **5**, 12120–12126.
58 J. Ding, Z. Su and H. Tian, *Ceram. Int.*, 2016, **42**, 12435–12440.
59 Z.-Q. Huo, Y.-T. Cui, D. Wang, Y. Dong and L. Chen, *J. Power Sources*, 2014, **245**, 331–336.
60 B. Wang, B. Xu, T. Liu, P. Liu, C. Guo, S. Wang, Q. Wang, Z. Xiong, D. Wang and X. S. Zhao, *Nanoscale*, 2014, **6**, 986–995.
61 J. Li, S.-H. Luo, Q. Wang, S. Yan, J. Feng, X. Ding, P. He and L. Zong, *J. Electrochem. Soc.*, 2019, **166**, A118–A124.
62 S. Li, X. Meng, Q. Yi, J. A. Alonso, M. T. Fernández-Díaz, C. Sun and Z. Wang, *Nano Energy*, 2018, **52**, 510–516.
63 M. B. Sahana, S. Vasu, N. Sasikala, S. Anandan, H. Sepehri-Amin, C. Sudakar and R. Gopalan, *RSC Adv.*, 2014, **4**, 64429–64437.
64 K. Saravanan, V. Ramar, P. Balaya and J. J. Vittal, *J. Mater. Chem.*, 2011, **21**, 14925.
65 Y. Lin, B. Zeng, Y. Lin, X. Li, G. Zhao, T. Zhou, H. Lai and Z. Huang, *Rare Met.*, 2012, **31**, 145–149.
66 Y. P. Huang, X. Li, Z. Chen, Y. Wu, Y. Chen, C. J. Kuang and S. X. Zhou, *Mater. Res. Innovations*, 2014, **18**, S4–2.
67 P. Zuo, G. Cheng, L. Wang, Y. Ma, C. Du, X. Cheng, Z. Wang and G. Yin, *J. Power Sources*, 2013, **243**, 872–879.
68 B. Luo, S. Xiao, Y. Li, Q. Xiao, Z. Li and G. Lei, *Mater. Technol.*, 2016, **32**, 1–7.
69 S.-M. Oh, H.-G. Jung, C. S. Yoon, S.-T. Myung, Z. Chen, K. Amine and Y.-K. Sun, *J. Power Sources*, 2011, **196**, 6924–6928.
70 P. Hohenberg and W. Kohn, *Phys. Rev.*, 1964, **136**, B864–B871.
71 G. Kresse and J. Furthmuller, *Phys. Rev. B: Condens. Matter Mater. Phys.*, 1996, **54**, 11169–11186.
72 G. Kresse and D. Joubert, *Phys. Rev. B: Condens. Matter Mater. Phys.*, 1999, **59**, 1758–1775.
73 J. P. Perdew, K. Burke and M. Ernzerhof, *Phys. Rev. Lett.*, 1996, **77**, 3865–3868.
74 H. J. Monkhorst and J. D. Pack, *Phys. Rev. B: Solid State*, 1976, **13**, 5188–5192.
75 X. Li, K. Zhang, D. Mitlin, E. Paek, M. Wang, F. Jiang, Y. Huang, Z. Yang, Y. Gong, L. Gu, W. Zhao, Y. G. Du and J. Zheng, *Small*, 2018, **14**, 1802570.
76 X. Li, Y. Tang, J. Song, W. Yang, M. Wang, C. Zhu, W. Zhao, J. M. Zheng and Y. Lin, *Carbon*, 2018, **129**, 236–244.
77 X. Li, K. Zhang, D. Mitlin, Z. Yang, M. Wang, Y. Tang, F. Jiang, Y. Du and J. Zheng, *Chem. Mater.*, 2018, **30**, 2566–2573.
78 X. Li, K. Zhang, S. Wang, M. Wang, F. Jiang, Y. Liu, Y. Huang and J. Zheng, *Sustainable Energy Fuels*, 2018, **2**, 1772–1780.
79 X. Li, K. Zhang, M. Wang, Y. Liu, M. Qu, W. Zhao and J. Zheng, *Sustainable Energy Fuels*, 2018, **2**, 413–421.
80 X. Li, J. Zheng, X. Ren, M. H. Engelhard, W. Zhao, Q. Li, J. Zhang and W. Xu, *Adv. Energy Mater.*, 2018, **8**, 1703022.
81 X. Li, Y. Liu, Y. Pan, M. Wang, J. Chen, H. Xu, Y. Huang, W. M. Lau, A. Shan, J. Zheng and D. Mitlin, *J. Mater. Chem. A*, 2019, **7**, 21349–21361.
82 O. Yariv, D. Hirshberg, E. Zinigrad, A. Meitav, D. Aurbach, M. Jiang and B. R. Powell, *J. Electrochem. Soc.*, 2014, **161**, A1422–A1431.
83 J. Zheng, P. Yan, W. H. Kan, C. Wang and A. Manthirama, *J. Electrochem. Soc.*, 2016, **163**, A584–A591.
84 C. Delmas, M. Maccario, L. Croguennec, F. L. Cras and F. Weill, *Nat. Mater.*, 2008, **7**, 665–671.
85 R. Dedryvère, M. Maccario, L. Croguennec, F. L. Cras, C. Delmas and D. Gonbeau, *Chem. Mater.*, 2008, **20**, 7164–7170.